Diamond & Related Materials 154 (2025) 112087

Contents lists available at ScienceDirect

Diamond & Related Materials

journal homepage: www.elsevier.com/locate/diamond

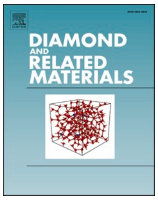

Compression of [121]Tetramantane to over 50 GPa - Phase transformations and elastic properties[☆]

Hendrik Heimes [1],[*], Jessica Wierbik, Jodie Bradby

Department of Materials Physics, Research School of Physics, The Australian National University, 60 Mills Rd, Acton 2601, ACT, Australia

ARTICLE INFO

Keywords:
High pressure
Phase transformation
Diamondoid
Tetramantane
Raman spectroscopy
Synchrotron X-ray diffraction
DFT

ABSTRACT

The hydrocarbon [121]tetramantane ($C_{22}H_{28}$) is a promising precursor material for the high-pressure high-temperature synthesis of nanodiamonds due its diamond-like carbon bonding network. We present a comprehensive study of its structural behaviour under pressure using single-crystal and synchrotron X-ray diffraction, Raman spectroscopy, and density functional theory calculations. At ambient conditions, [121]tetramantane crystallises in monoclinic space group $P2_1/n$ with lattice parameters of $a = 7.7192(1)$ Å, $b = 8.0112(1)$ Å, $c = 12.8281(2)$ Å, $\beta = 104.635(2)^\circ$, Z=2, and a density of 1.265(3) g/cm^3. Under non-hydrostatic diamond anvil cell compression, we observe two phase transitions: first to a phase with space group $P2/n$ at 1 GPa, followed by a transition to a high-pressure phase above 8 GPa indexed to a unit cell with space group $P2/m$ and lattice parameters $a = 14.62(1)$ Å, $b = 7.78(1)$ Å, $c = 6.39(1)$ Å, $\beta = 94.4(2)^\circ$, and Z=3, and a density of 2.010(3) g/cm^3 at 31 GPa. The isothermal bulk modulus B_0 increases significantly from the value of the ambient phase of (19.4 ± 0.9) GPa to that of the high-pressure phase of (147.5 ± 1.7) GPa. Upon recovery, [121]tetramantane transforms back to a $P2/n$ phase with similar lattice parameters compared to the initial $P2_1/n$ structure, but possesses significantly different relative peak intensities. This study provides valuable insights on the structure-property relationships of [121]tetramantane and suggests an optimal pressure of 8 GPa for the use of [121]tetramantane as a precursor for nanodiamond synthesis.

1. Introduction

Tetramantane ($C_{22}H_{28}$) belongs to an intriguing group of carbohydrates, the so-called diamondoids, which are molecules composed of fully sp^3-bonded carbon cages. The first report of a diamondoid dates back to 1933, when adamantane was first discovered and extracted from crude oil [1]. Over the years, it was found, that diamondoids are a common occurrence in petroleum as a thermal breakdown product of heavy hydrocarbons [2]. The smallest diamondoid, adamantane ($C_{10}H_{16}$), has a singular 10-atom carbon cage with the same atomic arrangement, bond lengths and bond angles compared to the smallest cage unit found in a pure carbon diamond lattice. By the addition of C_4H_4 units to the adamantane cage, higher-order diamondoids with a higher cage count are formed yielding the general chemical formula of diamondoids of $C_{4n+6}H_{4n+12}$ with n number of cages. Tetramantane (n=4) is considered the first higher diamondoid as it is the smallest possible diamondoid with different isomers. While two-caged diamantane ($C_{14}H_{20}$) and three-caged triamantane ($C_{18}H_{24}$) are mono-isomeric, the addition of a fourth diamondoid cage gives way to three geometrically different isomers, [1(2)3]tetramantane, [123]tetramantane and [121]tetramantane [3].

Due to their unique feature of possessing fully sp^3-bonded carbon cages, diamondoids have outstanding physical and chemical properties compared to regular hydrocarbons, such as high chemical inertness, high thermal stability, high molecular stiffness, and well-defined molecular sizes and shapes [3]. Furthermore, diamondoids can be functionalised [4], not only giving them a highly promising application as drug-delivery systems [5], but also raising the possibility of growing nanodiamonds with desirable defects in situ. For example, utilising an aza-adamantane ($C_9H_{15}N$) seed where one cage carbon in the adamantane molecule is substituted by nitrogen, fluorescent nanodiamonds can be synthesised [6] with myriad potential applications ranging from drug delivery systems and bioimaging [7] to quantum computing [8].

The unique fully sp^3-bonded carbon cage structure makes

[☆] This article is part of a special issue entitled: Ndnc2024 in Diamond & Related Materials.

[*] Corresponding author.

E-mail addresses: hendrik.heimes@anu.edu.au (H. Heimes), jessica.wierbik@anu.edu.au (J. Wierbik), jodie.bradby@anu.edu.au (J. Bradby).

[1] First author.

https://doi.org/10.1016/j.diamond.2025.112087
Received 20 December 2024; Received in revised form 3 February 2025; Accepted 6 February 2025

diamondoids highly interesting materials for high-pressure research. Park et al. (2020) [9] reported the formation of nanodiamonds at considerably lower pressure and temperature conditions using diamondoids in favour of conventional sp^2-bonded carbon and hydrocarbon precursors. Using a decomposable, reactive, organic compound as carbon supply, a GeI_4 catalyst, and adamantane as a seed, diamond growth conditions in a diamond anvil cell were reported to be pushed down as low as 3.5 GPa and 773 K [10], remarkably lower in both pressure and temperature compared to common high-pressure high-temperature diamond growth conditions from graphitic precursors of 5–6 GPa and 1573–1973 K [11,12].

Apart from their potential use as nanodiamond precursors, diamondoids were found to be excellent candidates for cushioning applications, outperforming conventional cushioning materials in both working pressure range and energy absorption density due to their rigid molecules interconnected by soft van der Waals forces [13]. Park et al. (2020) [14] published a study comparing numerous diamondoids and correlating their compressibility with the molecular shapes and arrangements, finding phase transformations in all analysed samples and concluding that lower H—H distances between individual molecules lead to phase transformations at lower pressures. Yang et al. (2014) [15] investigated the high-pressure behaviour of [121]tetramantane up to 20 GPa and found a phase transformation into a triclinic phase at 13 GPa, however no cell geometry and indexing of peaks was provided. Furthermore, the authors did not observe any anomalous mechanical behaviour of the sample.

This study revisits the high-pressure behaviour of [121]tetramantane, revealing previously unreported structural changes in [121] tetramantane, aiming to enrich the knowledge of diamondoids under high-pressure conditions, which is important for fine-tuning synthesis conditions of nanodiamonds from diamondoid precursors with numerous applications, as well as understanding the potential use of diamondoids for cushioning applications.

2. Material and methods

2.1. Single-crystal X-ray diffraction

Single-crystalline transparent [121]tetramantane with crystal sizes between 0.1 mm and 3 mm was provided by a collaborator. To unambiguously identify and analyse the structure of the sample and to check for possible impurities, single-crystal diffraction (SXRD) was employed. Measurements were carried out on a four-circle kappa diffractometer type SuperNova by Agilent Technologies with monochromated CuK_α-radiation and a Rigaku HyPix-6000HE Hybrid Photon Counting detector. The X-ray tube was operated at 50 kV and 40 mA with a full Ewald sphere scan. Measurements were performed at 298 K (RT) to obtain a structure refinement at ambient conditions and at 150 K (LT) to check for differences, as many molecular crystals are known to exhibit disorder phenomena at RT. Data reduction including analytical absorption correction was done with the CrysAlisPro software package (*V*.1.171.42.84a by Rigaku Oxford Diffraction) [21]. The structure determination was accomplished using *shelxt* (V. 2014/5) [22] with direct methods. The structure was refined using the software *shelxle* [23] with a non-linear least-squares procedure.

2.2. Generating high pressure

Boehler-Almax plate diamond anvil cells (DAC) equipped with Almax type IIa diamonds with culet diameters of 400 μm were used to generate high-pressure conditions of up to 54.5 GPa. Single-crystalline [121]tetramantane was crushed to a polycrystalline powder with grain sizes between 1 and 10 μm and was loaded in a sample chamber. Different sets of experiments utilising stainless steel (SS) and rhenium gaskets (Re) which were pre-indented to thicknesses of (50 ± 5) μm were carried out. Pressure calibration was carried out using the equation of state of gold fitted to the experimental in situ X-ray diffraction data, as well as using the Raman shift of the diamond anvil [16]. In the in situ Raman spectroscopy compression, a ruby ball with a 5 μm diameter was used as pressure calibrant and pressure was calculated based on the shift of the R1 ruby fluorescence line [17]. Uncertainties were estimated based on peak widths and wavenumber resolution of the Raman spectrometer.

2.3. Raman spectroscopy

Raman backscattering spectroscopy experiments were carried out utilising a Renishaw InVia Reflex Microscope. A 532 nm diode laser with a wavenumber resolution of 1.1 cm^{-1}, rejection edge filter of 30 cm^{-1} and maximum laser power after optics, before entering the anvils, of 5 mW, focussed down to a spot size of 2 μm and operated with a grating of 2400 l/mm was used.

2.4. In situ synchrotron powder X-ray diffraction

Synchrotron-based powder X-ray diffraction (S-PXRD) experiments were performed at the extreme conditions beamline P02.2 at DESY, Germany. Two sets of experiments in situ in diamond anvil cells were carried out, one utilising an SS gasket and an X-ray wavelength of 0.2909 Å focused down to a height of 7 μm and a width of 2 μm, and one utilising a Re gasket and an X-ray wavelength of 0.2926 Å focused down to a height of 8 μm and a width of 3 μm. The beamline was equipped with a Perkin Elmer XRD1621 detector with 2048 × 2048 pixels and a size of 200 × 200 $μm^2$. For calibration of the stage parameters, a CeO_2 standard was used. The recorded 2-dimensional scattering images were integrated to 1-dimensional scattering patterns utilising Dioptas *v*0.6.0 [18]. Peaks were indexed with GSAS-II v.5fbed4 [19], and lattice parameter refinement was performed via UnitCell (v.02/2006) [20].

2.5. Density functional theory (DFT) calculations

Raman spectra were calculated on a structure-optimised single [121] tetramantane molecule using the software package ORCA *v*. 5.0.4 [24] with the def2-SVP basis set [25], def2/J auxiliary basis [26] and B3LYP hybrid functional [27–30]. After ground state calculation via geometry optimisation, 3N-6 atom displacements were simulated representing all possible vibrational modes.

As the elastic stiffness of a structure plays a fundamental role in governing the reaction of the structure to applied pressures, the elastic stiffness tensor of [121]tetramantane was calculated via density functional theory (DFT). Calculations were performed utilising the .cif file obtained from RT SXRD as input with MedeA (v. 3.7) using the ab-initio total-energy and molecular dynamics package VASP (Vienna ab-initio simulation package) [31,32]. Two sets of calculations were done, the first one utilising general gradient approximation (GGA) with the PBEsol [33,34] functional with a plane wave cutoff of 400 eV and **k**-spacings of 0.210 $Å^{-1}$ × 0.196 $Å^{-1}$ × 0.127 $Å^{-1}$, the second one using the van der Waals corrected GGA functional revPBE-vdw [33,35] with a plane wave cutoff of 520 eV and **k**-spacings of 0.120 $Å^{-1}$ × 0.112 $Å^{-1}$ × 0.072 $Å^{-1}$. All atoms not fixed by symmetry with a greater than zero degree of freedom were relaxed with a convergence criterion of 0.02 eV/Å. The full elastic stiffness tensor $\{C_{ijkl}\}$ was calculated via the stress-strain relationship using an arbitrary strain of 0.005.

3. Results

3.1. Single-crystal X-ray diffraction

The crystal structure of [121]tetramantane at room temperature was solved and refined in space group $P2_1/n$ with lattice parameters of $a = 7.7192(1)$ Å, $b = 8.0112(1)$ Å, $c = 12.8281(2)$ Å and a monoclinic angle of $\beta = 104.635(2)^\circ$ with 2 formula units per unit cell (Z) yielding a density of 1.265(3) g/cm^3. For the final structure refinement, 965 unique reflections were refined using 157 parameters with a final R_1 value of 0.038 and a wR^2 of 0.129 and an excellent Goodness of Fit parameter (GooF) of 1.05. Hence, no systematic errors as well as no systematic residual between observed and calculated electron density were observed, indicating an absence of disorder phenomena within the single-crystal. Furthermore, the anisotropic temperature factors U_{ij} are not unusually large, and there are no negative displacement parameters U_{ii}. All C—C bonds have lengths between 1.517 Å and 1.543 Å, and all C—C angles are between 107.7° and 111.6°, typical for sp^3-bonded carbon, albeit slightly distorted. Individual [121]tetramantane molecules are bound via van der Waals forces with a minimal H—H distance between molecules of 2.46(3) Å.

At LT conditions of 150 K, the structure was successfully refined with an identical structure compared to ambient, with slightly smaller lattice parameters of $a = 7.6551(1)$ Å, $b = 7.9657(1)$ Å, $c = 12.7939(2)$ Å, $\beta = 104.892(2)^\circ$, and Z=2, yielding a density of 1.288(3) g/cm^3. For the final LT refinement, 945 unique reflections were refined using 157 parameters with a final R_1 value of 0.037 and a wR^2 of 0.120 and a GooF of 1.09. The full structure results including a complete list of all observed and indexed peaks can be found in the .cif files provided in supplementary data.

3.2. *Computational studies*

3.2.1. *Calculated vs experimental Raman spectrum*

The experimental Raman spectrum of the sample has the unique fingerprint of [121]tetramantane, reported by Filik et al. 2006 [36], with 72 of the 144 vibrational modes being Raman active due to its molecular symmetry of C_{2v}. The experimental spectrum can be well represented by DFT calculations with a single molecule as input (see Fig. 1). The calculation slightly overestimates the Raman shift in the higher wavenumber region, corresponding to C—H stretching vibrations. The use of correction factors may lead to more accurate results in this regime in future calculation attempts. Nevertheless, the DFT results enable the assignment of each peak to its respective vibrational mode, and indicate a negligible influence of the molecular crystal arrangement (i.e. the van der Waals forces between individual molecules) on the vibrational properties since all observed Raman modes can be perfectly represented by the vibration of a single molecule.

3.2.2. *Elasticity*

Results of the calculation of the elastic stiffness coefficients c_{ij} using Voigt notation are listed in Table 1. Both DFT GGA PBEsol and GGA revPBE-vdw approaches are in decent agreement regarding the general anisotropy of the elastic stiffness tensor. Molecular crystal structures with strong dependence on van der Waals interactions are known to be prone to produce largely variable absolute magnitudes of elastic properties with different DFT methods, with up to 50 % deviations, while generally giving a more reliable representation of the overall elastic anisotropy [37]. In the case of [121]tetramantane, the longitudinal stiffness c_{11}, c_{22} and c_{33} are in reasonable agreement, the transverse interactions c_{12}, c_{13} and c_{23}, as well as the coupling coefficients c_{15}, c_{25}, c_{35} and c_{46} are in excellent agreement, while the shear coefficients c_{44}, c_{55} and c_{66} are inconsistent. Therefore, both approaches can reasonably describe the longitudinal and transverse elastic response, whereas considerable uncertainties about the response to shear stresses remain. However, the solution provided by the GGA revPBE-vdw approach is most likely more accurate due to the correction for van der Waals interactions, the higher plane wave cutoff, and the finer mesh size used in

Table 1
DFT computed elastic coefficients c_{ij} (Voigt Notation) and Hill averages of bulk modulus B_H and shear modulus G_H of [121]tetramantane via GGA PBEsol and GGA revPBE-vdw functionals. The reported error bounds are obtained from the MT least-squares fitting algorithm and provide a measure of numerical uncertainty in the computed elastic coefficients.

quantity	GGA PBEsol (GPa)	GGA revPBE-vdw (GPa)
c_{11}	28.65 ± 1.84	30.16 ± 1.88
c_{22}	31.98 ± 1.84	37.46 ± 1.88
c_{33}	31.17 ± 1.84	31.93 ± 1.88
c_{44}	10.36 ± 2.61	25.27 ± 2.66
c_{55}	15.85 ± 1.84	15.46 ± 1.88
c_{66}	15.24 ± 1.84	27.16 ± 2.66
c_{12}	12.05 ± 1.30	13.49 ± 1.33
c_{13}	12.42 ± 1.30	13.60 ± 1.33
c_{15}	−7.89 ± 1.30	−7.70 ± 1.33
c_{23}	16.63 ± 1.30	16.52 ± 1.33
c_{25}	0.34 ± 1.30	0.42 ± 1.33
c_{35}	−12.99 ± 1.30	−12.51 ± 1.33
c_{46}	−7.90 ± 1.30	−8.59 ± 1.33
B_H	16.73	18.16
G_H	9.13	13.74

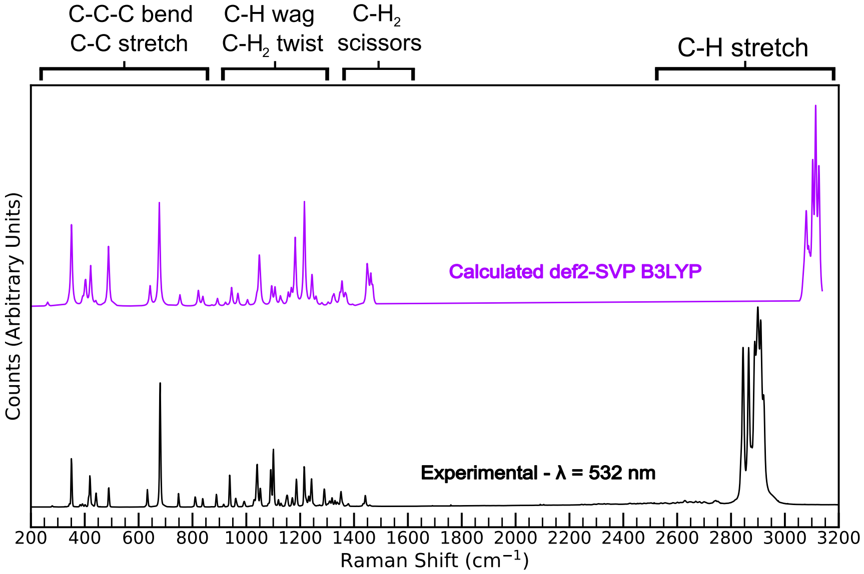

Fig. 1. Experimental Raman spectrum of a single-crystal [121]tetramantane and DFT calculated Raman spectrum of a single molecule [121]tetramantane, highlighting the negligible influence of the crystal structure on the vibrational properties of [121]tetramantane.

the computation.

The elastic stiffness tensor $\{C_{ijkl}\}$ obtained from the DFT calculations of [121]tetramantane were used to visualise the 3D representation of Young's modulus $\{E\}$ in a specified direction $\mathbf{d}$ (with direction cosines with $|\mathbf{d}| = 1$). The representation surfaces were determined using $E(\mathbf{d}) = \left(d_i d_j d_k d_l \{S_{ijkl}\}\right)^{-1}$, following Einstein's summation convention. Here, $\{S_{ijkl}\}$ represents the elastic compliance tensor derived through $\{C_{ijkl}\}^{-1} = \{S_{ijkl}\}$. $E(\mathbf{d})$ represents the material's stiffness in the direction $\mathbf{d}$ [38–40]. Fig. 2 shows the 3D representation of Young's modulus $\{E\}$ which highlights the considerable elastic anisotropy of [121]tetramantane resulting from both calculation approaches.

3.3. *High pressure studies*

3.3.1. *Optical observations*

Above pressures of 10 GPa, the sample chamber filled with [121] tetramantane underwent a drastic expansion lateral to the compression axis. This effect was especially significant in an SS gasket, where the gasket was almost fully pushed out of the anvil culet diameter at 18 GPa (see Fig. 3). Compressing [121]tetramantane in a mechanically more resilient Re gasket had a similar effect, albeit much less distinct.

3.3.2. *Split of Raman modes at high pressure conditions*

A full set of Raman spectra of [121]tetramantane at various pressure steps up to 25.6 GPa compressed in an SS gasket is presented in Fig. 4 a). Clear splits of Raman modes can be observed during the compression with the first recorded splits commencing at a pressure step of 1.3 GPa. In particular, the doubly degenerate cage shearing mode, which is situated at 350 cm^{-1} at 0 GPa, splits into two individual modes [see Fig. 4 b)]. A distinct split of the cage breathing mode which has a Raman shift of 680 cm^{-1} at 0 GPa, can be observed at a pressure step of 7.7 GPa [see Fig. 4 c)], albeit a faint emergence of a peak shoulder can already be observed at 5.4 GPa. At 9.9 GPa, the main cage breathing mode shifts towards slightly lower wavenumbers compared to the previous pressure step, while the newly emerged split peak gains intensity matching the intensity of the initial cage breathing mode. As the cage breathing mode is a non-degenerate vibrational mode, the formation of a new mode could imply a coexistence of two phases with a different molecular geometry. In the higher wavenumber region between 2800 cm^{-1} and 3100 cm^{-1} [see Fig. 4 a)], corresponding to C—H stretching vibrations, the relative intensities of the vibrational modes change between ambient conditions and the first pressure step, and again at 2.9 GPa.

A general trend of the pressure-dependent Raman spectra is the significant broadening and loss of intensity of peaks towards high pressures with almost all peaks indistinguishable from background above pressures of 20 GPa, except for the cage-breathing mode. As the characteristic Raman spectrum of [121]tetramantane results from the vibration of the individual molecules, this observation can be explained by the suppression of molecular vibration due to the significant reduction of intermolecular distances at high pressures and the shift from a solid characterised by weak van der Waals interactions to a lattice-like structure.

As the sample chamber with the SS gasket experienced a significant lateral expansion during compression, the maximum pressure achievable was limited to 25.6 GPa, and hence the experiment was repeated utilising a mechanically more resilient Re gasket up to a maximum pressure of 54.5 GPa. As mentioned in section 3.3.1, the sample chamber expanded at pressures above 10 GPa as well, albeit less pronounced. Fig. 5 shows the comparison of Raman spectra in the range of the cage breathing mode for the compression in SS and in Re at the edge of the sample chamber and the centre of the sample chamber. At the edge of the Re sample chamber, the pressure-dependent Raman shift of the cage breathing mode is comparable to the previous experiment in SS, with a slightly higher peak split onset of 7.7 GPa, and a full split at 10.5 GPa. At the centre of the sample chamber, however, the onset and full split of the cage breathing mode occurs at considerably higher pressures of 14.0 GPa and 24.2 GPa, respectively. This finding suggests a significant influence of local stress fields on the Raman active vibrational modes of [121]tetramantane. In the centre of the Re gasket sample chamber, the pressure conditions are most hydrostatic among all probed spots, while the SS compression is highly non-hydrostatic due to the significant lateral expansion of the sample chamber. Therefore, the cage mode split may be an indicator of highly non-hydrostatic stresses. Furthermore, the onset of the split of the cage breathing mode can be indicative of the beginning of the lateral expansion of the sample chamber in future experiments.

Remarkably, after decompression to ambient pressures, all peaks return to their original state with identical peak positions (see Fig. 6), indicating a full reversibility of intramolecular geometry after compression to a maximum pressure of 54.5 GPa. A plot of the pressure dependence of all recorded Raman modes up to 54.5 GPa is provided in supplementary data. In general, the modes shift more significantly as a function of pressure between 0 and 10 GPa, and almost linearly and less distinct beyond 10 GPa, which could be due to the decreasing intermolecular distances.

3.3.3. *X-ray diffraction*

Two sets of in situ S-PXRD experiments were carried out, using an SS and a Re gasket, respectively. Due to a large lateral expansion of the sample chambers, data were collected only up to 17 GPa in the SS gasket, and up to 31 GPa in the Re gasket. Compared to the Raman experiments

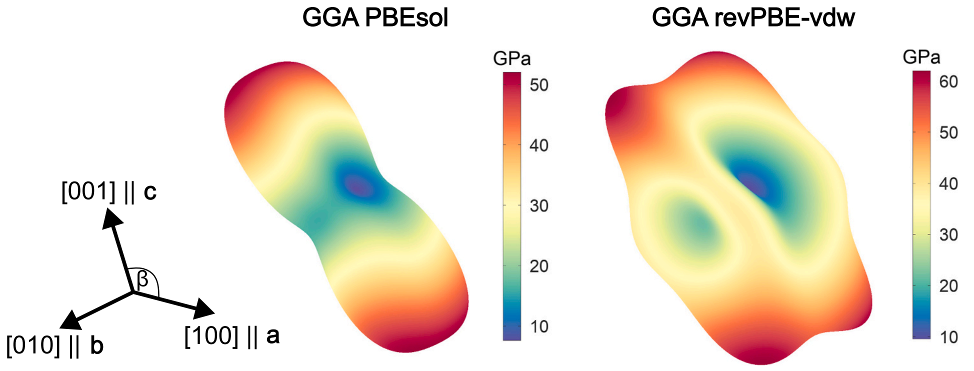

Fig. 2. 3D representation of Young's Modulus $\{E\}$ of [121]tetramantane computed by GGA PBEsol (left) and GGA revPBE-vdw (right). Note the slight difference in scale bars. Both approaches result in a similar anisotropy with the direction corresponding to [101] being least resistant to compression, while the direction corresponding to [10$\bar{2}$] is about 5 to 6 times stiffer. The difference between both results arises from the van der Waals interaction correction of the GGA revPBE-vdw approach, which likely gives a more detailed representation of the elasticity of [121]tetramantane, whereas the GGA PBEsol result represents a more simplified version. Images generated with VELAS [40].

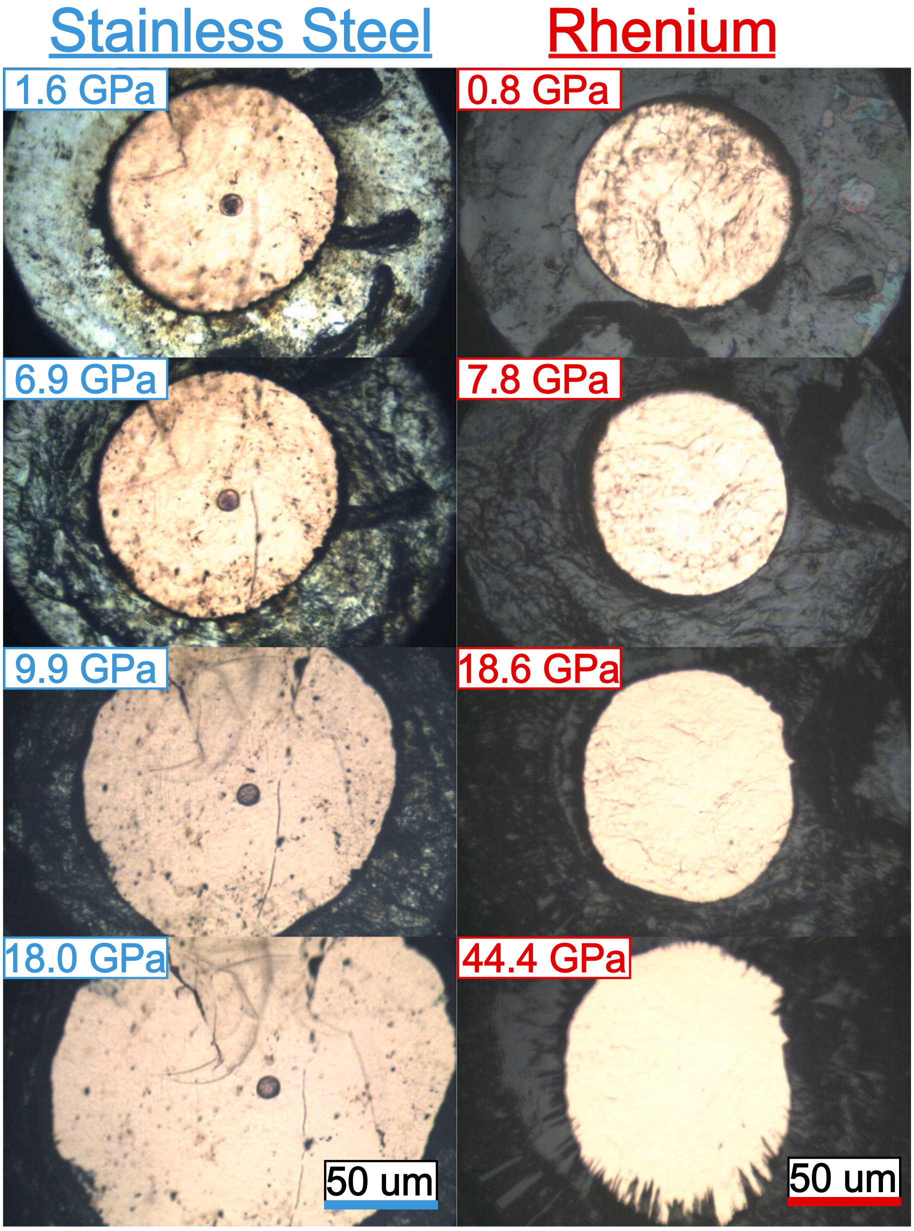

Fig. 3. Optical images taken with a Renishaw Raman inVia microscope with a 20× magnification lens through the top anvil of the diamond anvil cell (corresponding to the compression axis) utilising an SS gasket and a Re gasket. The sample chamber is illuminated from both the top, and the bottom side. In the centre of the SS sample chamber, a ruby ball used for pressure calibration can be seen. Starting from around 10 GPa, the sample chambers experience a considerable expansion perpendicular to the compression axis with the gasket material being pushed away. The effect is much more pronounced with SS as gasket material compared to Re.

the maximum pressure achieved was lower as the lateral expansion was more pronounced which could be explained by uncertainties in the gasket thickness measurements, or a slight overfilling of the cell with sample material. It is worth noting that due to the grain sizes of about 1 to 10 μm and beam sizes of $2 \times 7\ \mu m^2$ (SS) and $3 \times 8\ \mu m^2$ (Re), no perfect powder rings were recorded at all steps. Upon pressurising, clearer powder rings developed due to further crushing of grains within the cell. Example raw data images for boths runs at low, medium and high pressures are provided in supplementary data for reference. Fig. 7 shows the evolution of the XRD peaks of [121]tetramantane in both experiments. Due to the imperfect powder rings and grain size distribution, differences in relative intensities arise due to some of the strongest reflections being predominatly caused by single or very few large strained grains, causing an overrepresentation of those reflections in the integrated XRD patterns. Peaks of the initial monoclinic unit cell could be indexed and lattice parameter refinements were successfully carried out up to 13 GPa in SS, and 15.8 GPa in Re, however noting that at the first recorded pressure step in the SS experiments at 0.8 GPa, a novel peak at $q = 0.799(5)$ Å^{-1} with a corresponding lattice plane spacing of $d = 7.86$ (5) Å is present. As this lies almost within uncertainties of the calculated lattice parameter $b = 7.93(1)$ Å at this pressure step, this peak was indexed to (010). In Re, this (010) peak is present from 3.7 GPa onwards. As the (010) reflex is systematically absent in $P2_1/n$, the structure was indexed to $P2/n$ for consecutive pressure steps.

At 7.3 GPa in SS, and 8.1 GPa in Re, a new peak around $q \approx 0.77$ Å^{-1} was detected, marked with a green star in Fig. 7: This peak is incompatible with the original unit cell. At the following pressure steps of 10.0 GPa in SS, and 11.6 GPa and 15.8 GPa in Re, several other novel peaks emerge, and indexing a majority of the peaks utilising a single original unit cell is no longer possible. At 20 GPa in Re, several peaks that could be previously indexed to the original unit cell vanish, indicating a full completion of a phase change. Utilising the 31 GPa step of the Re

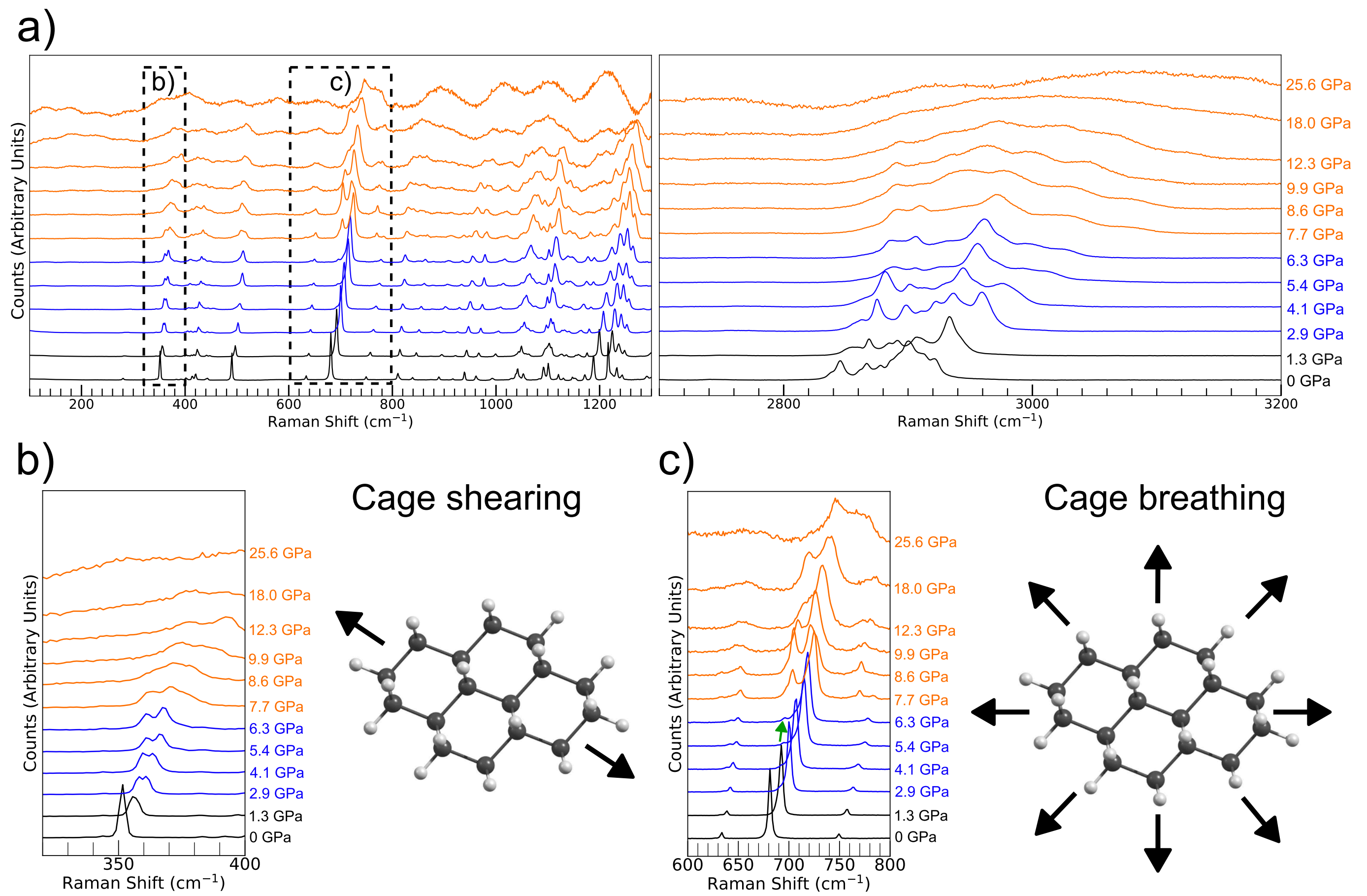

Fig. 4. a) Raman spectra of [121]tetramantane at pressure various steps from 0 GPa to 25.6 GPa. Blue-coloured spectra correspond to phases beyond the first observation of peak splits, while orange spectra correspond to phases after the split of the cage breathing mode. **b)** Clear split of the cage stretching Raman mode, situated at 350 cm^{-1} at ambient, into two individual modes at the second recorded pressure step of 2.9 GPa. **c)** The cage breathing mode, at 680 cm^{-1} at ambient, splits into two individual modes with an onset at 7.7 GPa. A faint shoulder already emerges above 5.4 GPa, marked with a green arrow.

experiment, the new phase was successfully indexed to a monoclinic cell with space group $P2/m$. Cell parameters were refined using 14 indexed reflections yielding a = 14.62(1) Å, b = 7.78(1) Å, c = 6.39(1) Å, β = 94.4(2)°, and Z=3, resulting in a cell volume V = (724.8 ± 1.1) Å^3 and a density of 2.010(3) g/cm^3. Utilising this cell geometry, phases at steps 11.6 GPa, 13.0 GPa, and 15.8 GPa were successfully attributed to a combination of the original phase and the new cell. The high intensity $(10\bar{1})$ and (101) reflections of the original cell are still present at 10.0 GPa and 13.0 GPa in SS, and 11.6 GPa and 15.8 GPa in Re, indicating a coexistence of two phases at this pressure regime. A table with unit cell parameters for each pressure step is provided in supplementary data.

The pressure-dependent volume V of both phases, with the volumes of the different phases normed to one [121]tetramantane molecule to enable comparison, is plotted in Fig. 8 a). The data was fitted with the Vinet and 3rd-order Birch-Murnaghan equation of state utilising the EosFit7 software [41] to calculate the isothermal bulk modulus B_0. The 3rd-order Birch-Murnaghan equation is defined as follows [42]:

$$P(V) = \frac{3B_0}{2}\left[\left(\frac{V_0}{V}\right)^{\frac{7}{3}} - \left(\frac{V_0}{V}\right)^{\frac{5}{3}}\right]\left\{1+\frac{3}{4}(B_p-4)\left[\left(\frac{V_0}{V}\right)^{\frac{2}{3}}-1\right]\right\} \tag{1}$$

with pressure P, the pressure derivative of the bulk modulus B_p, the unit cell volume V and the unit cell volume at 0 GPa V_0.

The Vinet equation of state is a modification of the Birch-Murnaghan equation of state and tends to perform better for highly compressible solids [43–45]:

$$P(V) = 3B_0\left(\frac{1-\eta}{\eta^2}\right) exp\left[\frac{3}{2}(B_p-1)(1-\eta)\right] \tag{2}$$

Here, η is defined as: $\eta = \left(\frac{V}{V_0}\right)^{\frac{1}{3}}$.

Axial stiffnesses were fitted with the same approach, utilising the pressure-dependent length change of the axes a, b, and c with respect to their lengths at 0 GPa a_0, b_0, and c_0 to obtain the axial stiffnesses M_0 and the pressure derivatives M_p. All equation of state fit results are listed in Table 2. For the low-pressure phase, the initial volume and axes lengths were fixed as the values obtained from SXRD results. The values for Vinet and 3rd-order Birch-Murnaghan fits agree within uncertainties, apart from axial stiffnesses of the b- and c-axis of the high-pressure phase. This may be caused by the rather high scatter of data points around the fit curve. In general, the uncertainties for the high-pressure phase are quite large, as the peaks are broad and a precise unit cell fit is not practicable. The a-axis of the high-pressure phase appears to be remarkably stiff with an axial stiffness M_p of over 600 GPa. Results for the low-pressure phase are plotted in Fig. 8 b) and for the high-pressure phase in Fig. 8 c). It is worth noting, that the equation of state fits of the low-pressure phase were done through data points including both $P2_1/n$ and $P2/n$ phases, and thus, the results are strictly speaking apparent bulk moduli, since the transition potentially affects the physical properties of the crystal. However, due to the similarities in XRD patterns and a continuous volume change, resulting in a smooth equation of state fit through all data points, the effect of the phase transition on the equation of state fits is likely minimal.

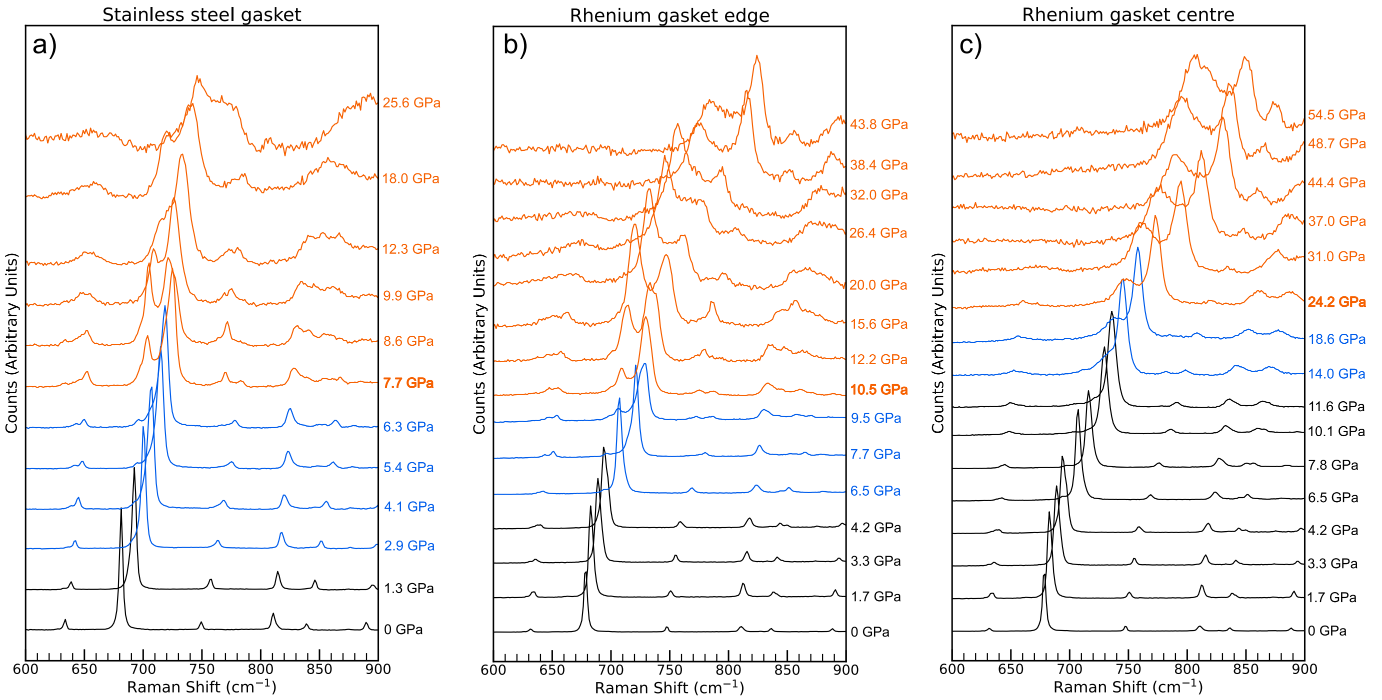

Fig. 5. Raman spectra of the cage breathing mode which resides at around 680 cm^{-1} at 0 GPa. Black spectra indicate pressure regions where a single mode is present, blue spectra indicate pressure regions where a satellite peak emerges, and orange spectra show pressure regions where a full split of the cage breathing mode is present. In the centre of an SS gasket sample chamber, the first satellite peak emerges at 5.4 GPa with a full split detected at 7.7 GPa (a). At the sample chamber edges in a Re gasket, the first satellite peak emerges at 7.7 GPa and a full split occurs at 10.5 GPa (b). In contrast, the satellite peak appears at 14.0 GPa and a full split occurs at 24.2 GPa at the centre of the sample chamber in a Re gasket (c).

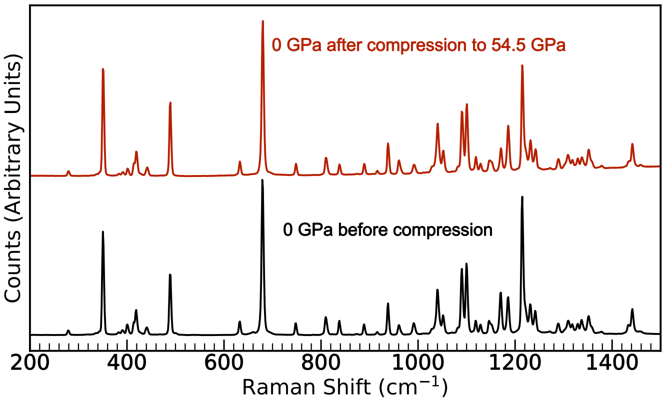

Fig. 6. Raman spectra taken before compression (black curve) and after compression to 54.5 GPa. Apart from one peak at 1170 cm^{-1}, all peak positions and relative intensities are identical, indicating a full recovery of molecular geometry after releasing pressure. A slight intensity difference in one vibrational mode at 1170 cm^{-1} may be due to the recovered sample being polycrystalline and randomly orientated, whereas the uncompressed spectrum was collected on a single-crystal with a specific orientation.

Upon unloading, the structure transforms back to $P2/n$. A clear (010) peak implies an absence of the 2_1 screw axis, and a considerable change in relative peak intensities compared to the uncompressed [121]tetramantane is present. The structure therefore does not reversibly transform into its original $P2_1/n$ structure. The lattice parameters of the recovered $P2/n$ phase are $a = 7.69(1)$ Å, $b = 8.02(1)$ Å, $c = 12.83(1)$ Å, $\beta = 105.07(2)^\circ$, and $Z = 2$, resulting in a cell volume $V = 763.5(2)$ Å^3, minimally smaller compared to the initial volume $V = 767.552(19)$ Å^3 of the uncompressed $P2_1/n$ structure.

4. Discussion

[121]tetramantane undergoes a series of phase transformations, the first of which occurs around 1 GPa and is associated with a loss of screw axis symmetry, changing the space group from $P2_1/n$ to $P2/n$. A second phase transformation to a high-pressure phase has a transition onset of around 8 GPa. Between the onset and about 17 GPa both low-pressure and high-pressure phases coexist. While both phase transformations are associated with a change in the long-range order, the geometry of individual molecules remains mostly unchanged due to the Raman modes, apart from few peak splits, experiencing no significant change. Beyond 17 GPa, no XRD peaks of the low-pressure phase can be detected, and thus, the phase transition to the high-pressure phase can be considered complete. At pressures exceeding the phase transformation onset of 8 GPa, the sample chamber starts expanding. Regions that experience the greatest deformation, i.e. the entire sample chamber in an SS gasket, and the edges of the sample chamber in a Re gasket, show a split of the non-degenerate cage breathing vibrational mode at pressures above the expansion onset. Fig. 9 shows a proposed mechanism as an explanation for the expansion. As the low-pressure phase has a strong elastic stiffness anisotropy [see Fig. 9 a)], the [121]tetramantane crystal grains likely realign with their structurally softest direction along [101] facing the compression axis due to the gasket material being softer than the diamond anvils. This in turn causes an increase in the monoclinic angle β which is the angle between the [100] and [001] axes [see Fig. 9 b)]. I.e. uniaxially compressing along [101] would cause an increase in β. Indeed, refined unit cells have a steady increase in β from 104.635(2)° to 107.0(5)° from ambient to 17 GPa [see Fig. 9 c)]. Furthermore, the phase recovered from high pressures has a strong preferential orientation compared to the initial uncompressed powder as the $(10\overline{1})$ and (101) reflections become very faint in the recovered phase [see Fig. 9 d)]. In a randomly orientated powder, as is approximately the case in the uncompressed sample, the $(10\overline{1})$ and (101) reflections are among the highest intensity peaks.

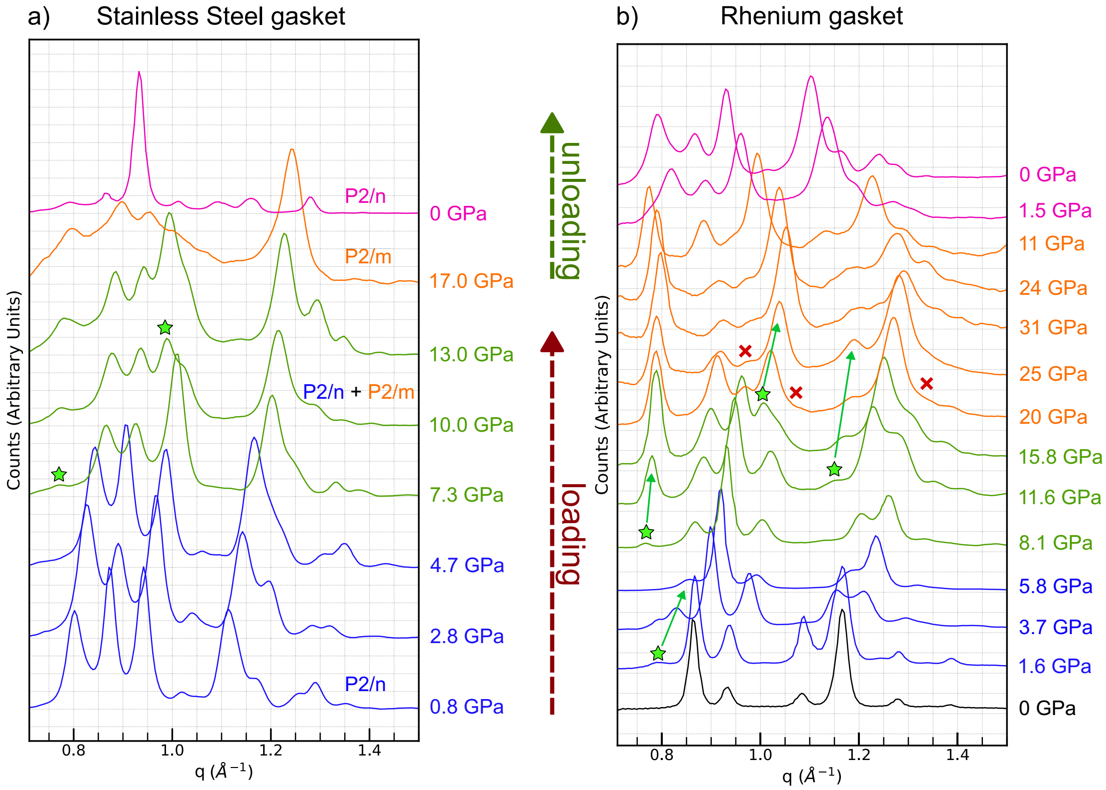

Fig. 7. Low **q**-range X-ray diffraction peaks of [121]tetramantane compressed in SS (a) and Re (b). Newly emerging peaks are marked with a green star and vanishing peaks are indicated by a red cross. The initial $P2_1/n$ structure transforms into a $P2/n$ structure at 0.8 GPa in the SS gasket experiment, which is characterised by the appearance of a (010) peak at around $q \approx 0.8$ Å^{-1}. This peak appears at 1.6 GPa in Re. At 7.3 GPa in SS and 8.1 GPa in Re, a phase transformation into a $P2/m$ phase starts, manifesting in the emergence of new peaks. At 17 GPa (a), and 20 GPa in (b), no peaks of the $P2/n$ structure remain, and the structure can be fully described by a $P2/m$ unit cell with a different cell geometry. Upon unloading, the structure transforms into a $P2/n$ phase with similar unit cell parameters to the original uncompressed structure, albeit with a significant shift in relative peak intensities. Note the difference in relative peak intensities between the phases recovered from the SS and Re gasket experiments, likely resulting from lateral gasket expansion and preferential reorientation of crystallites which was more pronounced in the SS gasket experiment.

After exceeding 8 GPa, the phase transformation into the high-pressure phase starts, and the structural changes associated with the transition may cause a lateral push on the gasket. It is worth noting that the high-pressure phase has significantly different mechanical properties compared to the low-pressure phase. Due to the different bulk modulus pressure derivatives of the low- and high-pressure phases, the bulk modulus at a pressure where both phases coexist enables a more accurate comparison. Therefore, the bulk modulus at a coexistence pressure $P = 15$ GPa was calculated from the equation of state fit parameters via $B(P) = B_0 + B_pP + \frac{1}{2}B_{pp}P^2$, resulting in (47.7 ± 4.6) GPa and (60.4 ± 4.6) GPa for the low-pressure phase, and (198.0 ± 3.4) GPa and (199.3 ± 3.4) GPa for the high-pressure phase, using the Vinet and 3rd-order Birch-Murnaghan fit results, respectively. The reason for this considerable difference in stiffness between low- and high-pressure phase likely roots in the significant reduction of intermolecular distances, and the practically incompressible individual molecules due to their diamond-like sp^3-bonded carbon cage structure. The high-pressure phase could thus be regarded as similar to a hydrogen-terminated diamond lattice, whereas the low-pressure phase is highly compressible due to the soft intermolecular van der Waals forces between molecules. Consequently, the transformation pressure threshold is a good indicator of the pressure regime where individual [121]tetramantane molecules are pushed close enough together to form a diamond-like lattice. Therefore, pressure conditions of around 8 GPa may be ideal for the synthesis of diamonds from [121]tetramantane precursors, with the addition of high temperatures locking in the structure, and removing C—H bonds.

A previous high-pressure study of [121]tetramantane by Yang et al. 2014 [15] found a bulk modulus value for the low-pressure phase of (5.45 ± 0.58) GPa with a 3rd-order Birch-Murnaghan equation of state fit, and (6.36 ± 0.18) GPa with a Vinet fit. The reported bulk moduli disagree with fit results for B_0 carried out in this study, as well as with the bulk modulus B_H obtained from DFT calculations. The authors reported considerably higher first derivatives of the bulk modulus with B_p of (18.75 ± 2.32) and (11.54 ± 0.21) compared to the fit results within this study of (4.3 ± 0.3) and (4.7 ± 0.3) via 3rd-order Birch-Murnaghan equation of state and Vinet equation of state fits, respectively. Utilising the reported values by Yang et al. 2014 [15], the data collected within our study can not be well represented, as the decrease in volume is too steep at low pressures, whereas it flattens too much at higher pressures compared to the experimental data. A possible reason for the discrepancies might be differences in pressure calibration. Yang et al. 2014 [15] reported utilising the ruby pressure gauge, which is only calibrated for hydrostatic pressure conditions. Within our study, pressure in the in situ XRD experiment was estimated based on a combination of the diamond anvil Raman shift, and shift of XRD peaks of a gold calibrant. The results reported in our study are based on fixing the V_0 value to 767.522 Å^3 as obtained from SXRD results. Yang et al. 2014 [15] fitted the value and reported significantly higher best-fit values of 782.80(5) Å^3 and 786.00(8) Å^3 via 3rd-order Birch-Murnaghan equation of state and Vinet equation of state fits, respectively. To cross-check, a final attempt at fitting the equation of state was done by freeing the V_0 parameter for refinement, leaving out the 15.8 GPa step of the Re experiment due to it potentially being an outlier, and fitting both Re and SS datasets simultaneously. The approach yields best-fit values of $V_0 = (775.6 \pm 1.1)$ Å^3, $B_0 = 18.00(16)$ GPa, and $B_p = 4.55(6)$ for the 3rd-order Birch-

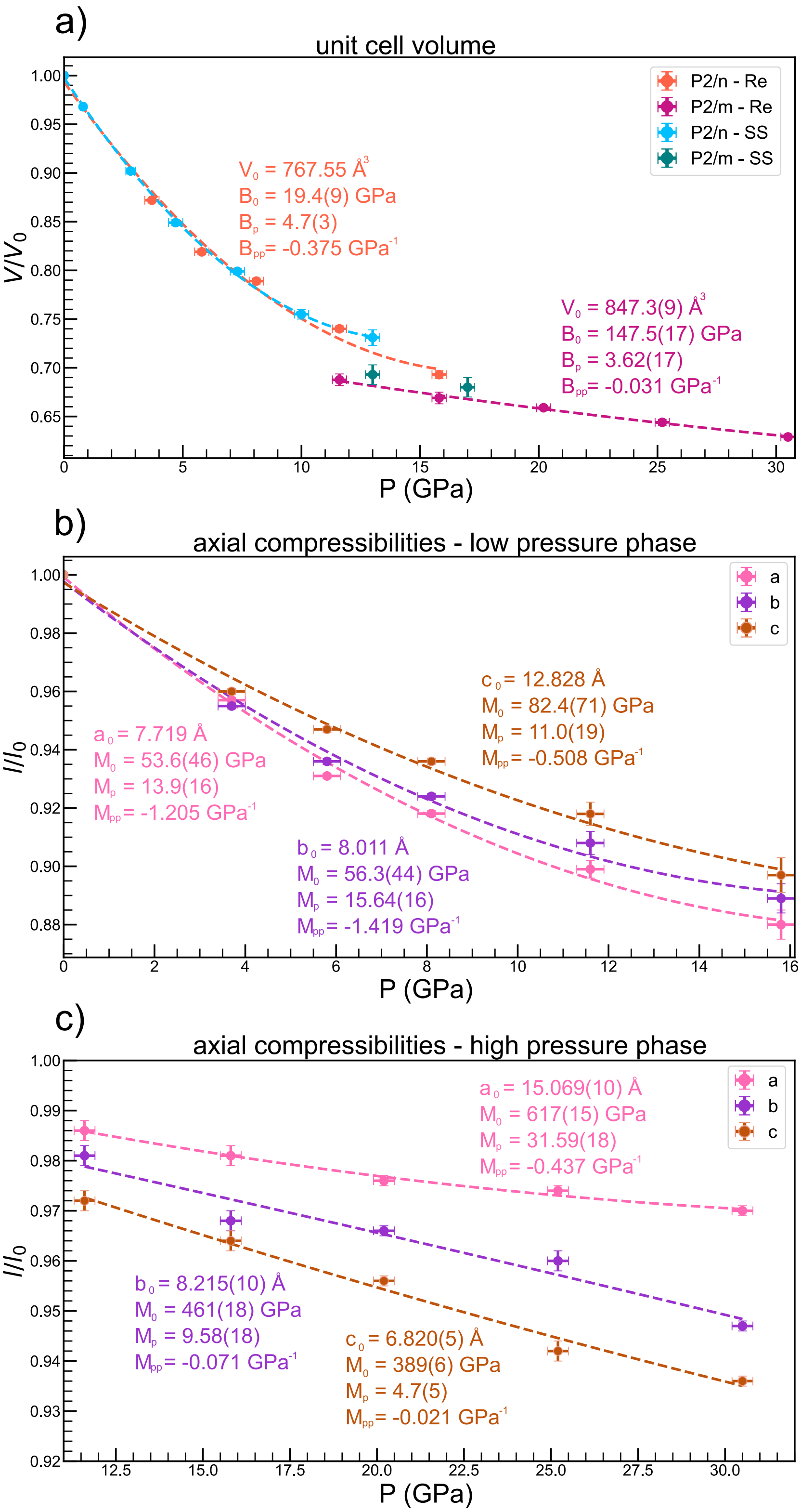

Fig. 8. **a)** Vinet equation of state fit to the pressure-dependent volume V of the unit cell of [121]tetramantane. Data from SS gasket and Re gasket experiments are in good agreement. V/V_0 data of the high-pressure phase was normed to V_0 of the low-pressure phase based on the volume of one formula unit per elementary cell for each phase to keep consistency. **b)** Vinet equation of state fit to the pressure-dependent axial lengths of the low-pressure phase unit cell of [121]tetramantane compressed in a Re gasket. **c)** Vinet equation of state fit to the pressure-dependent axial lengths of the high pressure phase unit cell of [121]tetramantane compressed in a Re gasket.

Table 2

Vinet and 3rd-order Birch-Murnaghan (BM3) equation of state fit results for both low- and high-pressure phases of [121]tetramantane, for both volumetric, and axial changes. Indices (0) refer to values at 0 GPa, indices (*p*) are the first derivatives as a function of pressure. Indices (*pp*) are the second pressure derivatives which are implied values from the fit and therefore have no uncertainties.

	low-pressure phase		high-pressure phase	
	Vinet	BM3	Vinet	BM3
V_0 (Å^3)	767.522	767.522	847.3 ± 0.9	846.9 ± 0.9
B_0 (GPa)	19.4 ± 0.9	19.9 ± 0.9	147.5 ± 1.7	149.5 ± 1.7
B_p	4.7 ± 0.3	4.3 ± 0.3	3.6 ± 0.2	3.5 ± 0.2
B_{pp} (GPa^{-1})	−0.375	−0.213	−0.031	−0.024
a_0 (Å)	7.719	7.719	15.069 ± 0.010	15.070 ± 0.002
M_0 (GPa)	53.6 ± 4.7	55.0 ± 4.3	617 ± 15	613 ± 15
M_p	13.9 ± 1.7	12.8 ± 1.3	31.6 ± 1.8	33.9 ± 2.4
M_{pp} (GPa^{-1})	−1.205	−0.688	−0.437	−0.952
b_0 (Å)	8.011	8.011	8.215 ± 0.010	8.200 ± 0.098
M_0 (GPa)	56.3 ± 4.5	57.9 ± 4.6	461 ± 18	573 ± 19
M_p	15.6 ± 1.6	14.3 ± 1.6	9.6 ± 1.8	2.9 ± 1.1
M_{pp} (GPa^{-1})	−1.419	−0.814	−0.071	−0.159
c_0 (Å)	12.828	12.828	6.820 ± 0.005	6.831 ± 0.005
M_0 (GPa)	82.4 ± 7.1	83.4 ± 6.2	389 ± 6	356 ± 5
M_p	11.0 ± 1.9	10.5 ± 1.3	4.7 ± 0.5	7.3 ± 0.4
M_{pp} (GPa^{-1})	−0.508	−0.393	−0.021	−0.121

Murnaghan equation of state and $V_0 = (776.7 \pm 1.1)$ Å^3, $B_0 = 17.34(15)$ GPa, and $B_p = 4.98(7)$ for the Vinet equation of state, similar to the previously obtained values.

Yang et al. 2014 [15] reported a phase transition into a triclinic *P*1 phase above 13 GPa with a bulk modulus of (126.00 ± 12.25) GPa and (123.84 ± 11.88) GPa using 3rd-order Birch-Murnaghan and Vinet equation of state fits, respectively. The authors have not provided information on the unit cell metric of this phase, and within the limits of our study, observed peaks of the high-pressure phase could not be adequately described by a *P*1 unit cell with similar volumes to the low-pressure phase at transition pressure. As new peaks emerge at a lower *q*-values compared to the low-pressure phase, corresponding to larger *d*-spacings, an increase in cell volume is implied. Nevertheless, the bulk modulus of the high-pressure phase given by Yang et al. 2014 [15] is similar to the bulk modulus B_0 of the high-pressure phase found within our study. Therefore, the phases could be structurally related. However, without in situ high-pressure SXRD data, it is not possible for our work to determine the exact structure of [121]tetramantane due to the ambiguity in indexing few PXRD peaks in low symmetry space groups.

Upon unloading, Yang et al. 2014 [15] found [121]tetramantane to transform into a structure with space group *Pc* and unit cell parameters $a = 7.689(2)$ Å, $b = 8.045(2)$ Å, $c = 13.167(3)$ Å, $\beta = 109.3(3)^\circ$, and $V = 769.0(2)$ Å^3. The peaks observed at $d = 7.23(1)$ Å and 5.70(1)Å of the recovered phase from our study are incompatible with the *Pc* spacegroup. However, the peaks can be indexed as $(10\overline{1})$ and (101) reflections in space group $P2/n$ with lattice parameters $a = 7.69(1)$ Å, $b = 8.02(1)$ Å, $c = 12.83(1)$ Å, $\beta = 105.07(2)^\circ$, and $V = 763.5(2)$ Å^3, which adequately describes all observed reflections. Furthermore, this unit cell metric is very close to that of the uncompressed $P2_1/n$ structure. This indexing works for recovered samples from both Re and SS gasket experiments. The Raman spectrum of the recovered phase was found to be identical to the uncompressed $P2_1/n$ phase, indicating an identical molecular geometry of the recovered phase compared to the uncompressed phase. Hence, the observed difference between the initial and recovered phase arises from a difference in the long-range order of molecules, and not from a change of the structure within the molecules. It is possible that [121]tetramantane molecules can crystallise in several geometrically different arrangements with different crystal structures, which are energetically close to one another. Depending on the specific deviatoric stresses from hydrostaticity on each individual cell loading, [121]tetramantane could potentially lock into different metastable, but energetically close crystal structures. Experiments carried out in perfectly hydrostatic environments would be desirable. However, it is worth noting that the use of pressure-transmitting media is difficult in the case of molecular crystals due to the possibility of gases and liquids diffusing in between individual molecules, and thus changing the compressibility of the molecular crystal structure, possibly hindering the compaction of molecules. It might be worth testing the feasibility of using a soft solid-state pressure medium such as NaCl. However, due to [121]tetramantane being very soft at low pressures itself, solid-state-pressure media may introduce undesirable non-hydrostatic stresses too. For future experiments, we suggest the use of even softer solid-state materials as pressure-transmitting media, such as plasticine.

5. Conclusions

This study shows that [121]tetramantane has a complex high-pressure response. Pressures above 10 GPa with significant non-hydrostatic stress components may hinder successful nanodiamond synthesis from [121]tetramantane due to competing molecular arrangements. Remarkably, despite compression to 54.5 GPa and substantial structural changes, [121]tetramantane's molecular structure completely recovers upon decompression, demonstrating the considerable structural integrity of the diamondoid cage molecules. Furthermore, our work reveals that non-hydrostatic compression can uncover unique structural properties, while the choice of gasket material significantly impacts the pressure conditions within the sample chamber. The high-pressure phase exhibits unusual mechanical properties, displaying remarkable stiffness for a hydrocarbon and likely causing the observed anomalous lateral expansion. The observed phenomena may however be concerning when considering [121]tetramantane for cushioning applications, as the crystal structure does not fully revert back to its original state upon decompression. Instead, the material could be suitable to act as an emergency pressure trigger, as the sample chamber expands once the phase transformation pressure threshold to the high-pressure phase is reached. As the high-pressure phase is quite stiff, the individual molecules are likely pushed close enough together to form a lattice-like structure. Therefore, pressures above 8 GPa, with the addition of high temperatures to lock in the compacted structure, may be ideal to synthesise nanodiamonds from [121]tetramantane. High degrees of non-hydrostatic stresses above 10 GPa could introduce undesirable disorder and defects into the synthesis product due to the intramolecular strain observed via Raman spectroscopy. To fully understand the structural evolution of [121]tetramantane, future studies should employ high-pressure SXRD to determine the complete structure of the high-pressure phase. Such experiments need to carefully consider the use of an appropriate pressure-transmitting medium, due to a possible diffusion of liquids and gases in between the molecules, and the potential introduction of non-hydrostatic stresses from a solid-state pressure medium.

CRediT authorship contribution statement

Hendrik Heimes: Writing – review & editing, Writing – original draft, Visualization, Methodology, Investigation, Formal analysis, Conceptualization. **Jessica Wierbik:** Writing – review & editing, Methodology, Formal analysis. **Jodie Bradby:** Writing – review & editing, Supervision, Project administration, Methodology, Funding acquisition.

Declaration of competing interest

The authors declare the following financial interests/personal relationships which may be considered as potential competing interests:

Hendrik Heimes reports financial support was provided by Australian Nuclear Science and Technology Organisation. Jessica Wierbik reports financial support was provided by Australian Nuclear Science and

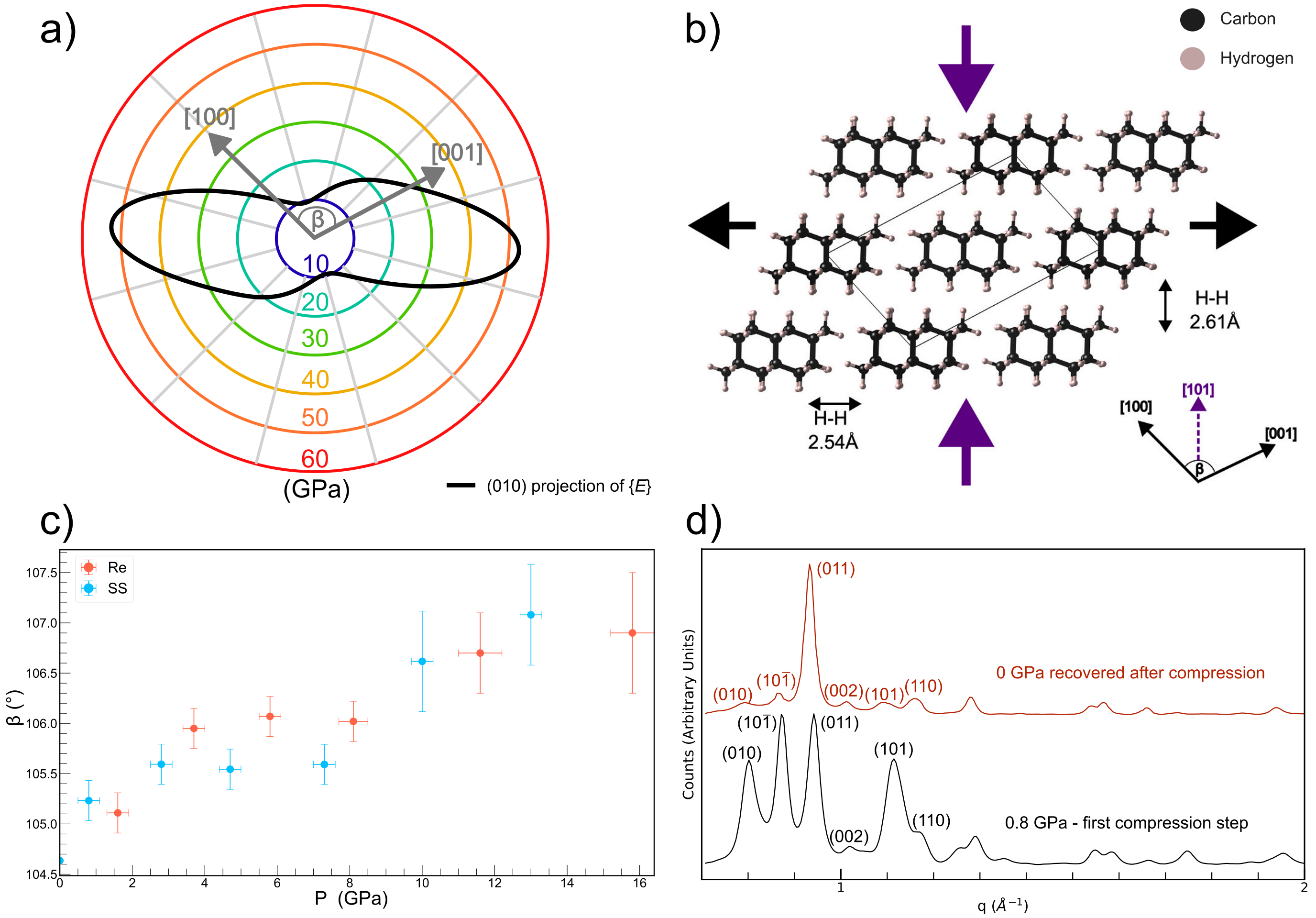

Fig. 9. **a)** (010) projection of the Youngs Modulus $\{E\}$ of [121]tetramantane, exhibiting a distinct elastic stiffness minimum along [101]. **b)** Proposed mechanism for the transverse expansion in [121]tetramantane: Under non-hydrostatic pressure, the crystal structure predominantly aligns with the [101] direction facing the compression axis, causing a transverse expansion (black arrows) with regard to the compression axis (purple arrows). As the onset of the transverse expansion correlates with a phase transformation observed by in situ XRD and Raman spectroscopy, the mechanism described above could be the main trigger of the transformation. Crystal structure drawn in VESTA [46] using the .cif file resulting from SXRD structure refinement. **c)** The monoclinic angle β in dependence of pressure P. β significantly increases upon compression which can be explained by a higher compressibility along the [101] direction of the crystal. I.e. a uniaxial compression along [101] leads to an increase of β. **d)** S-PXRD data of the experiment conducted in the SS gasket provides further evidence for the proposed mechanism as the sample recovered from compression has a significantly reduced peak intensity of the (101) and $(10\bar{1})$ reflections.

Technology Organisation. If there are other authors, they declare that they have no known competing financial interests or personal relationships that could have appeared to influence the work reported in this paper.

Acknowledgements

We acknowledge DESY (Hamburg, Germany), a member of the Helmholtz Association HGF, for the provision of experimental facilities. Parts of this research were carried out at PETRA III and we would like to thank Nico Giordano for assistance in using the P02.2 Extreme Conditions Beamline. Beamtime was allocated for proposal I-20230434 and I-20240136. We acknowledge travel funding provided by the International Synchrotron Access Program (ISAP) managed by the Australian Synchrotron, part of ANSTO, and funded by the Australian Government. We thank Philip R. Hemmer and Alastair Stacey for providing the [121] tetramantane crystals used in this research. We thank Dougal McCulloch, Alan Salek and Xingshuo Huang for assisting during synchrotron X-ray diffraction experiments. This research was supported by an AINSE Ltd. Postgraduate Research Award (PGRA).

Appendix A. Supplementary data

Supplementary data to this article can be found online at https://doi.org/10.1016/j.diamond.2025.112087.

Data availability

Data will be made available on request.

References

[1] S. Landa, V. Machacek, Adamantane, a new hydrocarbon extracted from petroleum, Collect. Czechoslov. Chem. Commun. 5 (1933) 1–5, https://doi.org/10.1135/cccc19330001.

[2] J.E. Dahl, J.M. Moldovan, K.E. Peters, G.E. Claypool, M.A. Rooney, G.E. Michael, M.R. Mello, M.L. Kohnen, Diamondoid hydrocarbons as indicators of natural oil cracking, Nature 399 (1999) 54–57, https://doi.org/10.1038/19953.

[3] K.-W. Yeung, Y. Dong, L. Chen, C.-Y. Tang, W.-C. Law, G.C.-P. Tsui, Nanotechnology of diamondoids for the fabrication of nanostructured systems, Nanotechnol. Rev. 9 (2020) 650–669, https://doi.org/10.1515/ntrev-2020-0051.

[4] M.A. Gunawan, J.-C. Hierso, D. Poinsot, A.A. Fokin, N.A. Fokina, B.A. Tkachenko, P.R. Schreiner, Diamondoids: functionalization and subsequent applications of perfectly defined molecular cage hydrocarbons, New J. Chem. 38 (2014) 28–41, https://doi.org/10.1039/C3NJ00535F.

[5] A. Štimac, M. Šekutor, K. Mlinarić-Majerski, L. Frkanec, R. Frkanec, Adamantane in drug delivery systems and surface recognition, Molecules 22 (2) (2017) 297, https://doi.org/10.3390/molecules22020297.

[6] M. Alkahtani, J. Lang, B. Naydenov, F. Jelezko, P. Hemmer, Growth of high-purity low-strain fluorescent nanodiamonds, ACS Photonics 6 (2019) 1266–1271, https://doi.org/10.1021/acsphotonics.9b00224.

[7] V. Vaijayanthimala, D.K. Lee, S.V. Kim, A. Yen, N. Tsai, D. Ho, Nanodiamond-mediated drug delivery and imaging: challenges and opportunities, Expert Opin. Drug Deliv. 12 (5) (2014) 735–749, https://doi.org/10.1517/17425247.2015.992412.

[8] M.W. Doherty, N.B. Manson, P. Delaney, F. Jelezko, J. Wrachtrup, L.C. L. Hollenberg, The nitrogen-vacancy colour centre in diamond, Phys. Rep. 528 (2013) 1–45, https://doi.org/10.1016/j.physrep.2013.02.001.

[9] S. Park, I.I. Abate, J. Liu, C. Wang, J.E.P. Dahl, R.M.K. Carlson, L. Yang, V. B. Prakapenka, E. Greenberg, T.P. Deveraux, C. Jia, E.R. Ewing, W.L. Mao, Y. Lin, Facile diamond synthesis from lower diamondoids, Sci. Adv. 6 (2020), https://doi.org/10.1126/sciadv.aay9405.

[10] J. Liang, C.P. Ender, T. Zapata, A. Ermakova, M. Wagner, T. Weil, Germanium iodide mediated synthesis of nanodiamonds from adamantane seeds under moderate high-pressure high-temperature conditions, Diam. Relat. Mater. 108 (2020) 108000, https://doi.org/10.1016/j.diamond.2020.108000.

[11] F.P. Bundy, H.P. Bovenkerk, H.M. Strong, R.H.W. Jr, Diamond-graphite equilibrium line from growth and graphitization of diamond, J. Chem. Phys. 35 (1961) 383–391, https://doi.org/10.1063/1.1731938.

[12] E.A. Ekimov, M.V. Kondrin, Chapter six - high-pressure, high-temperature synthesis and doping of nanodiamonds, Semiconductors and Semimetals 103 (2020) 161–199, https://doi.org/10.1016/bs.semsem.2020.03.006.

[13] F. Yang, Y. Lin, M. Baldini, J.E.P. Dahl, R.M.K. Carlson, W.L. Mao, Effects of molecular geometry on the properties of compressed diamondoid crystals, J. Phys. Chem. Lett. 7 (2016) 4641–4647, https://doi.org/10.1021/acs.jpclett.6b02161.

[14] S. Park, Y. Lin, W.L. Mao, in: C.E. Manning, J.-F. Lin, W.L. Mao (Eds.), Diamondoids under pressure, carbon in earth's interior, 2020, https://doi.org/10.1002/9781119508229.ch27.

[15] F. Yang, J.E.P. Dahl, R.M.K. Carlson, W.L. Mao, High pressure raman and X-ray diffraction study of [121] tetramantane, J. Phys. Chem. C 118 (2014) 7683–7689, https://doi.org/10.1021/jp500431k.

[16] Y.A.H. Kawamura, Pressure calibration of diamond anvil raman gauge to 410 GPa, J. Phys. Conf. Ser. 215 (2010) 012195, https://doi.org/10.1088/1742-6596/215/1/012195.

[17] G. Shen, Y. Wang, A. Dewaele, C. Wu, D.E. Fratanduono, J. Eggert, S. Klotz, K. F. Dziubek, P. Loubeyre, O.V. Fatyanov, P.D. Asimov, T. Mashimo, R.M. M. Wentzcovitch, Towards an international practical pressure scale: a proposal for an ipps ruby gauge (ipps-ruby2020), High Pressure Res. 40 (2020) 299–314, https://doi.org/10.1080/08957959.2020.1791107.

[18] C. Prescher, V.B. Prakapenka, Dioptas: a program for reduction of two-dimensional X-ray diffraction data and data exploration, High Pressure Res. (2015) 223–230, https://doi.org/10.1080/08957959.2015.1059835.

[19] B.H. Toby, R.B.V. Dreele, Gsas-ii: the genesis of a modern open-source all purpose crystallography software package, J. Appl. Crystallogr. 46 (2013) 544–549, https://doi.org/10.1107/S0021889813003531.

[20] T.J.B. Holland, S.A.T. Redfern, Unit cell refinement from powder diffraction data: the use of regression diagnostics, Min. Mag. 61 (1997) 65–77, https://doi.org/10.1180/minmag.1997.061.404.07.

[21] R.O. Difraction, Crysalispro Software Package, 2015.

[22] G.M. Sheldrick, A short history of shelx, Acta Crystallogr. A 64 (2008) 112–122, https://doi.org/10.1107/S0108767307043930.

[23] C.B. Hübschle, G.M. Sheldrick, B. Dittrich, Shelxle: a qt graphical user interface for shelxl, J. Appl. Crystallogr. 44 (2011) 1281–1284, https://doi.org/10.1107/S0021889811043202.

[24] F. Neese, The orca program system—version 5.0, WIREs Comput Mol Sci. 12 (2022) e1606, https://doi.org/10.1002/wcms.1606.

[25] F. Weigend, R. Ahlrichs, Balanced basis sets of split valence, triple zeta valence and quadruple zeta valence quality for h to rn: design and assessment of accuracy, Phys. Chem. Chem. Phys. 7 (2005) 3297, https://doi.org/10.1039/B508541A.

[26] F. Weigend, Accurate coulomb-fitting basis sets for h to rn, Phys. Chem. Chem. Phys. 8 (2006) 1057, https://doi.org/10.1039/B515623H.

[27] A.D. Becke, Density-functional thermochemistry. III. The role of exact exchange, J. Chem. Phys. 98 (1993) 5648–5652, https://doi.org/10.1063/1.464913.

[28] C. Lee, W. Yang, R.G. Parr, Development of the colle-salvetti correlation-energy formula into a functional of the electron density, Phys. Rev. B 37 (1988) 785–789, https://doi.org/10.1103/PhysRevB.37.785.

[29] S. Vosko, L. Wilk, M. Nusair, Accurate spin-dependent electron liquid correlation energies for local spin density calculations: a critical analysis, Can. J. Phys. 58 (1980) 1200–1211, https://doi.org/10.1139/p80-159.

[30] P. Stephens, F. Devlin, C. Chabalowski, M. Frisch, Ab initio calculation of vibrational absorption and circular dichroism spectra using density functional force fields, J. Phys. Chem 98 (1994) 11623–11627, https://doi.org/10.1021/j100096a001.

[31] G. Kresse, J. Furthmüller, Efficient iterative schemes for ab initio total-energy calculations using a plane-wave basis set, Phys. Rev. B 54 (1996) 11169, https://doi.org/10.1103/PhysRevB.54.11169.

[32] G. Kresse, J. Furthmüller, Efficiency of ab-initio total energy calculations for metals and semiconductors using a plane-wave basis set, Comput. Mater. Sci. 6 (1996) 15–50, https://doi.org/10.1016/0927-0256(96)00008-0.

[33] J.P. Perdew, K. Burke, M. Ernzerhof, Generalized gradient approximation made simple, Phys. Rev. Lett. 77 (1996) 3865, https://doi.org/10.1103/PhysRevLett.77.3865.

[34] J.P. Perdew, A. Ruzsinszky, G.I. Csonka, O.A. Vydrov, G.E. Scuseria, L. A. Constantin, X. Zhou, K. Burke, Restoring the density-gradient expansion for exchange in solids and surfaces, Phys. Rev. Lett. 100 (2008), https://doi.org/10.1103/PhysRevLett.100.136406.

[35] Y. Zhang, W. Yang, Comment on "generalized gradient approximation made simple", Phys. Rev. Lett. 80 (1998) 890, https://doi.org/10.1103/PhysRevLett.80.890.

[36] J. Filik, J. Harvey, N. Allan, P. May, J. Dahl, S. Liu, R. Carlson, Raman spectroscopy of diamondoids, Spectrochemica Acta Part A 64 (2006) 681–692, https://doi.org/10.1016/j.saa.2005.07.070.

[37] K.M. Bal, A. Collas, Are elastic properties of molecular crystals within reach of density functional theory? Accuracy, robustness, and reproducibility of current approaches, ASC Publications 24 (2024), https://doi.org/10.1021/acs.cgd.4c00026.

[38] J.F. Nye, Physical Properties of Crystals, Oxford University Press, New York, 2006.

[39] J. Nordmann, M. Aßmus, H. Altenbach, Visualising elastic anisotropy: theoretical background and computational implementation, Cont. Mech. Thermody. 30 (2018) 689–705, https://doi.org/10.1007/s00161-018-0635-9. https://doi.org/10.1007/s00161-018-0635-9.

[40] Z. Ran, C. Zou, Z. Wei, H. Wang, Velas: an open-source toolbox for visualization and analysis of elastic anisotropy, Computer Phys. Comm. 283 (2023) 108540, https://doi.org/10.1016/j.cpc.2022.108540. https://www.sciencedirect.com/science/article/pii/S0010465522002594.

[41] R.J. Angel, J. Gonzalez-Platas, M. Alvaro, Eosfit7c and a fortran module (library) for equation of state calculations, Z. Kristallogr. 229 (2014) 405–419, https://doi.org/10.1515/zkri-2013-1711.

[42] F. Birch, Finite elastic strain of cubic crystals, Phys. Rev. 71 (1947) 809, https://doi.org/10.1103/PhysRev.71.809.

[43] P. Vinet, J. Ferrante, J.R. Rose, An universal equation of state for solids, J. Phys. Chem. 19 (1986) 467–473, https://doi.org/10.1088/0022-3719/19/20/001.

[44] P. Vinet, J. Ferrante, J.R. Rose, Compressibility of solids, J. Geophys. Res. 92 (1987) 9319–9325, https://doi.org/10.1029/JB092iB09p09319.

[45] P. Vinet, J. Ferrante, J.R. Rose, Temperature effects on the universal equation of state of solids, Phys. Rev. B 35 (1987) 81945–81953, https://doi.org/10.1103/PhysRevB.35.1945.

[46] K. Momma, F. Izumi, Vesta 3 for three-dimensional visualization of crystal, volumetric and morphology data, J. Appl. Crystallogr. 44 (2013) 1272–1276, https://doi.org/10.1107/S0021889811038970.